nature cities

Article

https://doi.org/10.1038/s44284-025-00302-1

Urban meteorology–chemistry coupling in compound heat–ozone extremes

Received: 5 February 2025

Accepted: 15 July 2025

Published online: 15 August 2025

Check for updates

Xueyu Zhou[1,2], Mengmeng Li[1,2], Xin Huang[1,2] ✉, Tengyu Liu[2], Haoran Zhang[2], Ximeng Qi[3,4], Zilin Wang[1,2], Yue Qin[5], Guannan Geng[6], Jiaping Wang[1,2], Xuguang Chi[1,2] & Aijun Ding[1,2,4]

Heatwaves and ozone (O_3) pollution threaten human and ecosystem health, with their compounding effects particularly severe in cities. While ground-based observations are indicative of urban O_3 pollution during heatwaves, limited vertical insights into the intensified and prolonged O_3 pollution hinder a comprehensive understanding of the underlying mechanisms and mitigation strategies. Here, leveraging airship vertical measurements and meteorology–chemistry coupled modeling, we reveal that heatwave-reinforced turbulence redistributes precursors vertically, altering photochemical stratification and accelerating O_3 production both at the surface and aloft over megacities in China. Stringent emission controls targeting nitrogen oxides could mitigate the heatwave-exacerbated O_3 extremes by narrowing the vertical disparity of photochemical sensitivity. Although heatwaves are projected to intensify, emission reductions due to China's carbon neutrality pledge could alleviate urban O_3 pollution by 41–47% during heatwaves and help tackle the dual challenges of air pollution and global warming while enhancing the climate resilience of city clusters.

Climate change has been escalating the intensity and frequency of heatwaves, with detrimental effects on human health, agriculture and ecosystems[1,2]. Heat extremes, defined as single days with daily maximum temperature (T_{max}) exceeding the 90th percentile in this study, often coincide with severe ozone (O_3) pollution, as strong sunlight, little rainfall and stagnant air under high-pressure systems facilitate the accumulation of both air pollutants and heat[3]. Exposure to concurrent heatwaves and O_3 extremes poses threats to human health, particularly for cities due to overlapping socioeconomic, demographic and climatic factors[4].

O_3 is predominantly formed via complex and nonlinear photochemical reactions of nitrogen oxides (NO_x) and volatile organic compounds (VOCs)[5]. Heatwaves and O_3 extremes are intricately linked and have been extensively studied based on surface observations[6–8]. During heatwaves, soaring temperatures and intense sunlight accelerate the chemical kinetic rates of photochemical O_3 production[9]. High temperatures also exacerbate ground-level O_3 by triggering a surge of biogenic volatile organic compound (BVOC) emissions from vegetation, particularly from highly temperature-sensitive herbaceous species in urban landscapes[10]. Furthermore, heatwaves drive soil drying and decrease the stomatal conductance of vegetation, thereby weakening dry deposition and worsening O_3 pollution near the surface[11].

Beyond the interconnections near the surface, long-lasting and widespread heatwave-associated O_3 pollution usually extends into the upper air[12]. Existing studies demonstrate that O_3 exhibits heterogeneous vertical profiles largely determined by multiple physical and chemical processes, such as stratospheric intrusion[13], synoptic situations[14] and planetary boundary layer (PBL) dynamics[15], as well as nonlinear photochemistry[16]. Meanwhile, heatwaves feature a positive temperature anomaly spanning the troposphere with intensity varying

[1]State Key Laboratory of Severe Weather Meteorological Science and Technology, Nanjing University, Nanjing, China. [2]Joint International Research Laboratory of Atmospheric and Earth System Sciences, School of Atmospheric Sciences, Nanjing University, Nanjing, China. [3]Nanjing-Helsinki Institute in Atmospheric and Earth System Sciences, Nanjing University, Suzhou, China. [4]Frontiers Science Center for Critical Earth Material Cycling, Nanjing University, Nanjing, China. [5]College of Environmental Sciences and Engineering, Peking University, Beijing, China. [6]State Key Joint Laboratory of Environmental Simulation and Pollution Control, School of Environment, Tsinghua University, Beijing, China. ✉e-mail: xinhuang@nju.edu.cn

https://doi.org/10.1038/s44284-025-00302-1

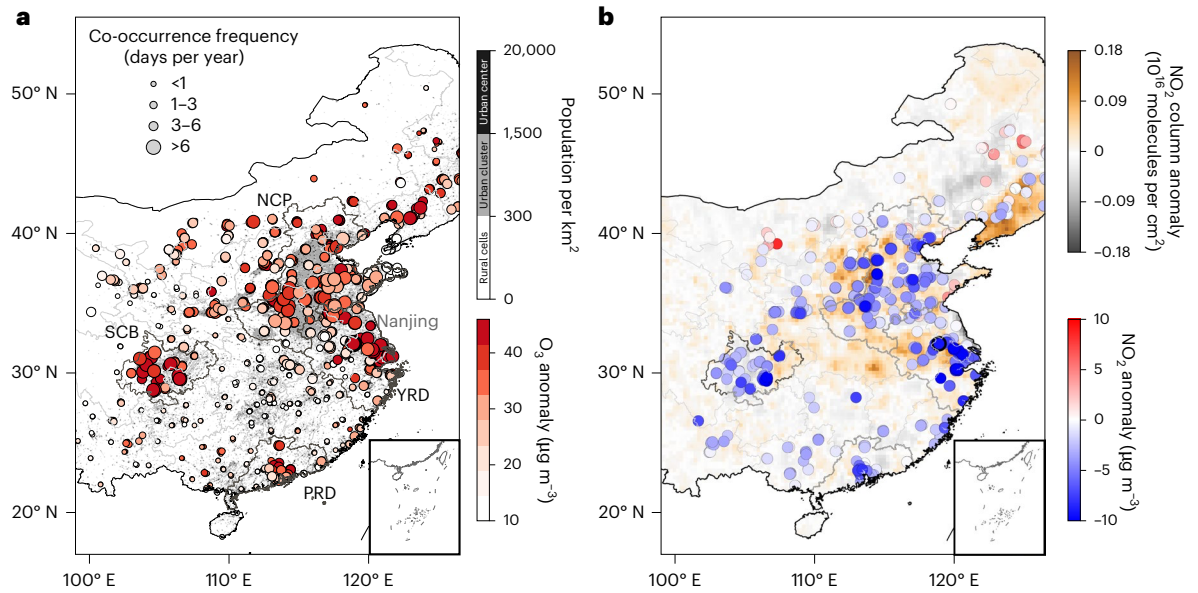

Fig. 1 | Heatwave-associated O_3 and NO_2 anomalies in main city clusters of China. a, The difference in MDA8 O_3 concentrations between heatwave days and normal days (red dots, sized by the frequency of concurrent heatwave and O_3 pollution) during May–August from 2014 to 2023. The shaded gray area shows the gridded population density and three types of grid cells classified by the degree of urbanization[50]. **b**, The difference in tropospheric NO_2 column densities from satellite retrievals (shaded contour) and surface NO_2 concentrations in the afternoon (12:00–16:00 LT) at sites with O_3 anomalies greater than 30 μg m^{-3} (dots) between heatwave days and normal days during May–August from 2014 to 2023.

greatly across altitudes[17], which affects the magnitude of near-surface heat[18] and, consequently, O_3 levels. However, vertical insights into the photochemical stratification and intricate connection between heatwaves and O_3 are relatively limited owing to sparse vertical observations, and a comprehensive mechanism understanding is imperative to cope effectively with such compound extremes.

Rapid urbanization and industrialization have led to substantially increased warming and O_3 pollution across the Northern Hemisphere over recent decades[19]. With one-sixth of the world's population and the fastest urbanization process globally[20], China is among the regions most severely affected by compound heat–O_3 extremes, especially in highly populated megacities. Unlike Europe and the United States where O_3 levels have declined due to emission controls, O_3 pollution in China deteriorates continuously, with warm-season daily maximum 8 h average (MDA8) O_3 increasing by 1.4 ± 1.2 ppb per year during 2013–2022 (ref. 21). With a warming rate nearly twice the global average[22] and expanding urban growth, China is exceptionally sensitive to climate extremes. As urbanization and climate warming intensify heatwaves and further exacerbate O_3 pollution[23], tackling these dual challenges of climatic extremes and air pollution is an urgent need.

In this study, we integrate satellite and ground observations, a specially designed airship campaign, and meteorology–chemistry coupled modeling to disentangle the underlying mechanisms of heatwave-associated O_3 pollution from a vertical perspective. Furthermore, we assess the potential of targeted emission reductions to mitigate urban photochemical pollution in a warming climate, offering critical insights for future climate and air quality strategies tailored for cities in China and other regions facing similar dual challenges.

Heatwave-associated ozone pollution and vertically heterogeneous anomalies

In China, O_3 pollution events with MDA8 O_3 exceeding China's Ambient Air Quality Standards Grade II of 160 μg m^{-3} occur frequently during the warm season (May–August), and most of them are linked to heat extremes. Observations from air quality monitoring networks over the past decade (2014–2023) illustrate a widespread O_3 enhancement during heatwaves (Fig. 1a). The average MDA8 O_3 concentration increases from 106.9 μg m^{-3} on normal days to 131.8 μg m^{-3} during heatwaves. The proportion of sites with O_3 exceedances more than doubled, rising from 11.5% to 26.6% during heatwaves. These positive O_3 anomalies are particularly evident in densely populated and industrialized city clusters such as the North China Plain (NCP), the Yangtze River Delta (YRD), the Pearl River Delta (PRD) and the Sichuan Basin (SCB) (Fig. 1a). Among these regions, YRD experienced the most prominent O_3 increment, reaching 37.6 μg m^{-3}. The co-occurrence frequency of warm-season O_3 and heatwaves (defined as the days with both T_{max} and MDA8 O_3 exceedances) in these highly populated city clusters has surpassed 4.2 days per year over the past decade (Fig. 1a), increasingly endangering city dwellers and the urban environment.

NO_x is a vital precursor of urban O_3 formation and originates mainly from industry, transportation and power generation in cities[24]. During heatwaves, NO_x also exhibits notable anomalies characterized by substantial vertical contrasts (Fig. 1b). The satellite-retrieved tropospheric NO_2 column densities show an obvious increase, possibly due to elevated NO_x emissions from soil and industrial sources[25,26]. In contrast, surface NO_2 concentrations show a negative anomaly, resulting in a seemingly conflicting shift of NO_x that is particularly evident in the YRD megacity cluster. Such vertical disparities provide new insights into the linkages between heatwaves and vertical stratification of photochemical ozone pollution. However, current measurements on photochemically active species are predominantly ground-based rather than for the urban boundary layer, which fail to grasp the full scope of the underlying processes involved in compound heat and O_3 extremes.

To comprehensively understand the physical and chemical mechanisms of compound heat and O_3 extremes, we conducted an intensive airship field campaign near the Station for Observing Regional Processes of the Earth System (SORPES) in Nanjing, a megacity in YRD with frequent heatwaves and O_3 pollution, in the early summer (May–June) of 2023 (Extended Data Fig. 1a). We deployed in situ instruments mounted on a rack underneath the airship to provide highly time-resolved observations of O_3 and its precursors (NO_x and VOCs), as well as key meteorological parameters (Methods and Extended Data Fig. 1b). At the same time, real-time surface measurements with a wide range

https://doi.org/10.1038/s44284-025-00302-1

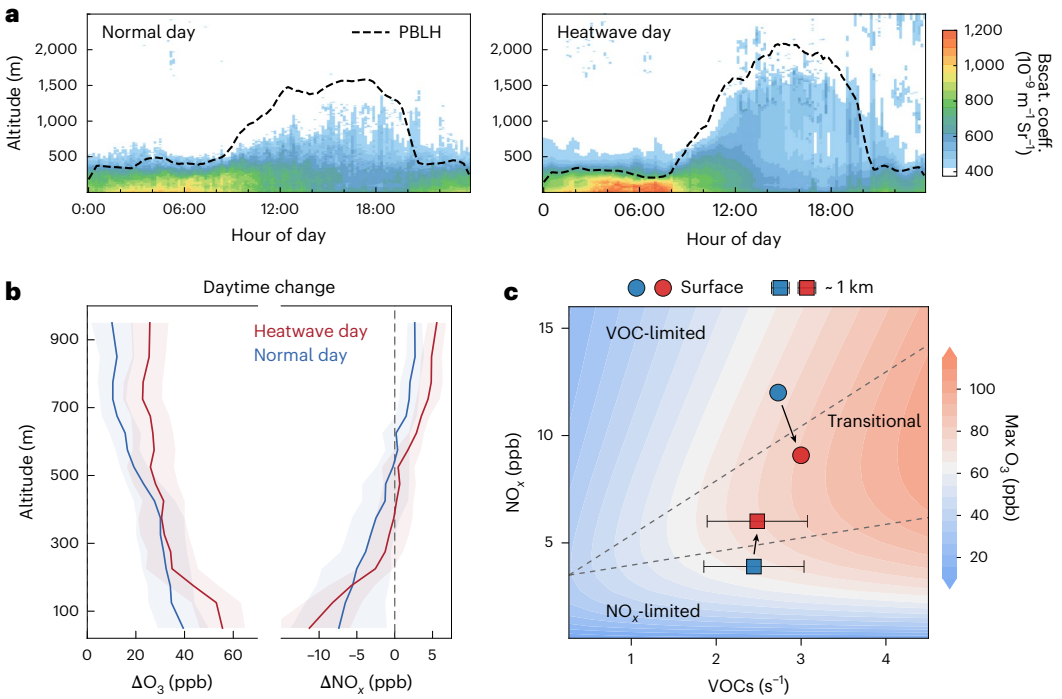

Fig. 2 | Responses of urban boundary layer, O_3 and NO_x to heatwaves. a, The averaged backscattering coefficient (Bscat. coeff.) and PBLH from the ceilometer on normal days and heatwave days at the SORPES station in May–June 2023. **b**, Daytime evolution in O_3 and NO_x profiles from the morning (7:00–9:00 LT) to afternoon (12:00–16:00 LT). The solid lines represent mean values and shaded areas show the 25–75th percentiles. **c**, An isopleth diagram of daily maximum O_3 against daytime NO_x concentration and VOC reactivity. The circles indicate the mean value of NO_x concentration and VOC reactivity at the surface on normal days (blue circle) and heatwave days (red circle). The squares represent the mean value of NO_x concentration and VOC reactivity near 1,000 m and the error bars show ± 50% s.d. of VOC reactivity. There are 27 observation points for VOC observation near 1,000 m.

of photochemistry-related species and meteorological parameters were also conducted at SORPES. In total, 197 vertical profiles were recorded from the surface to a maximum altitude of 1,200 m during the 2 month campaign experiment. On the basis of these measurements, O_3 pollution did show a tight link with high temperatures (Extended Data Fig. 1c). This experiment thus provides vertical insights into the photochemical and boundary layer processes involved in O_3 pollution in a typical urban environment.

As there is less cloud cover and soil evapotranspiration during heatwave days, more heat is released into the air, reinforcing the high air temperature and convective turbulence[27–29] (Extended Data Fig. 2). Therefore, the urban boundary layer usually fully develops during heatwaves, which is well reflected by anomalously high planetary boundary layer height (PBLH) and strong turbulent mixing (Fig. 2a). Accordingly, during heatwave days, airship-measured NO_x vertical profiles show quite distinct daytime evolution, which feature a notable increase (2.91 ppb) aloft, while a distinct decline (−3.89 ppb) near the surface (Fig. 2b). This vertical heterogeneity of NO_x agrees well with the long-term records in Fig. 1b. Such pronounced vertical changes in NO_x concentration result from the fact that heat-enhanced convection fuels turbulent mixing and the uplift of anthropogenic emissions, which even outweigh NO_x emission increases from industrial sources or soil volatilization owing to high temperatures[25,26]. This is further supported by a relatively lower surface NO_x concentration observed during heatwave afternoons (that is, 4.17 ppb), compared with 7.13 ppb on warm-season normal days (Extended Data Fig. 3).

On the other hand, the O_3 concentration rises at both the surface and aloft during heatwaves (Fig. 2b). That is, O_3 shows a synchronous increase with NO_x in the upper air but changes oppositely near the surface. Here, the altitude-dependent O_3 response to NO_x was mainly attributed to the vertical heterogeneity of VOC concentrations relative to NO_x (Extended Data Fig. 4a,b), which governs the regime of O_3 photochemical formation. As shown in Fig. 2c, the photochemical O_3 regime gradually shifts from VOC-sensitive to NO_x-sensitive with altitude owing to the vertical stratification of NO_x and VOCs[16,30]. In the NO_x-sensitive upper boundary layer, heatwaves supplement NO_x by stronger convection and fuel O_3 photochemical production. Near the surface where photochemical production of O_3 is predominantly VOC-sensitive, heatwaves elevate BVOC emissions and the ambient isoprene level (from 1.4 to 2.9 ppb; Extended Data Fig. 4c), while also stimulating the vertical dispersion of near-surface NO_x (from −5.9 ppb to −12.0 ppb; Extended Data Fig. 3a), contributing to a notable increment in daytime O_3 chemical production (from 5.5 to 10.6 ppb h^{-1}). Overall, the airship measurements indicate that, by reallocating precursors vertically, heatwaves shift the stratification of photochemical regime and facilitate O_3 formation both near the surface and in the upper boundary layer, jointly exacerbating O_3 pollution.

Vertical stratification of photochemical responses to heatwaves

To quantitatively understand the key physical and chemical mechanisms in heatwave-enhanced O_3 pollution, coupled meteorology–chemistry simulations with process diagnosis were performed using a single-column model (SCM) version of Weather Research and Forecasting model coupled with Chemistry (WRF–Chem) (Methods). Two groups of simulations (each including three parallel experiments) were conducted, driven by heatwave and normal meteorological conditions, respectively. As shown in Extended Data Fig. 5, the simulations are capable of capturing the meteorological differences between heatwave and normal days. The modeling results indicate that heatwaves elevate the vertical O_3 levels by reinforcing photochemical production, which can further be disentangled into three key pathways. Specifically, heatwaves favor O_3 formation directly through accelerating photochemical reaction rates under higher temperatures and radiation

https://doi.org/10.1038/s44284-025-00302-1

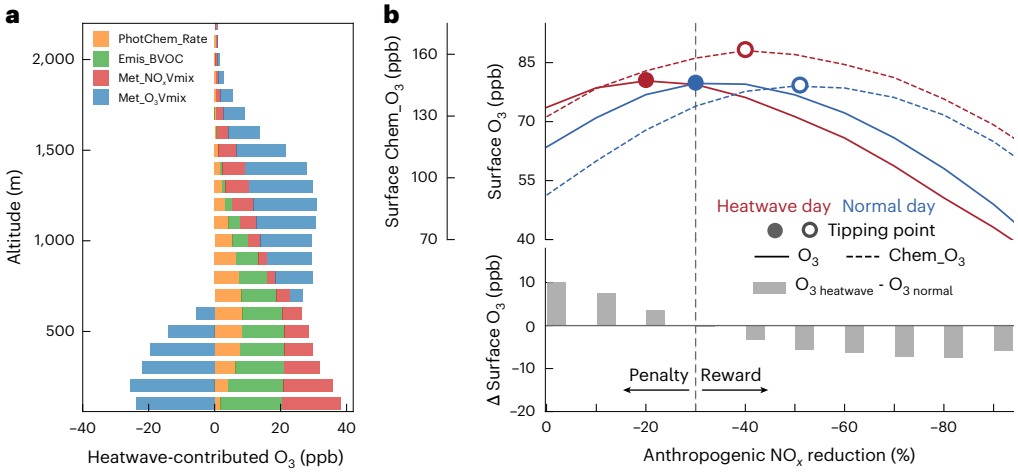

Fig. 3 | Heatwave-induced O_3 anomalies through different pathways and the responses to anthropogenic NO_x emission reductions. a, Diagnostic process contributions to heatwave-induced daytime (10:00–16:00 LT) O_3 changes in Nanjing simulated by SCM. Met_O_3Vmix represents the reinforced turbulence mixing of O_3 owing to heatwaves; PhotChem_Rate, Emis_BVOC and Met_NO_xVmix represent heatwave-enhanced chemical production of O_3 from accelerating photochemical reaction rates, boosting biogenic emissions and redistributing anthropogenic precursors, respectively. **b**, The response of surface daytime O_3 enhancement (solid lines) and chemical formation contributions (Chem_O_3, dotted lines) (<100 m) to reductions in anthropogenic NO_x emission. The solid and hollow circles indicate the tipping points where O_3 mitigation and photochemical regime transition, respectively. The red and blue lines represent the heatwave and normal scenarios, respectively. The gray bars show the difference between the two scenarios, representing heatwave-induced O_3 changes, with positive values indicating heatwave penalties and negative values signifying heatwave rewards.

(PhotChem_Rate) and indirectly by boosting biogenic VOC emissions (Emis_BVOC). In addition, consistent with the airship observation, heatwaves tend to vertically redistribute the precursor profiles, particularly NO_x (Met_NO_xVmix), which modulates O_3 photochemical production. The magnitude and relative contribution of three chemical pathways vary greatly with altitude owing to the vertical stratification of O_3 photochemical regime (Fig. 3a). Near the surface (<100 m), precursor redistribution and biogenic emissions have comparable contributions, accounting for 46.7% and 48.8% of enhanced O_3 production, respectively. However, in the middle boundary layer, the accelerated photochemical reaction becomes increasingly pronounced, peaking at nearly 31.9% around 600 m. At higher altitudes (1,000–1,500 m), during heatwaves, supplemental NO_x from the uplift of near-surface emissions dominates the enhancement in O_3 chemical formation (60.5%). The enhanced near-surface O_3 chemical production, together with vertical transport, jointly drives O_3 elevation at higher altitudes where precursors are limited. Such elevated O_3 aloft could be kept in the residual layer overnight with negligible chemical and deposition loss, exacerbating surface O_3 pollution after the residual layer breaks up the following morning[15].

Given the vital role of NO_x precursors in both the surface and upper air, anthropogenic emissions could influence urban O_3 pollution by altering photochemical regimes. Under high ambient NO_x levels in megacities of China (for example, Nanjing), initial NO_x reductions would enhance O_3 chemical production near the surface and decrease it aloft owing to the aforementioned vertical disparities of the photochemical sensitivity regime. As emission reductions increase, both O_3 production at the surface and aloft would be NO_x-sensitive, where limited NO_x availability will sharply reduce O_3 levels (Fig. 3b and Extended Data Fig. 6).

Heatwaves help remove surface NO_x and supplement upper NO_x, thereby advancing the tipping point of surface photochemical regime transition and O_3 mitigation by 10% in terms of NO_x reductions (Fig. 3b). This suggests that while heatwaves exacerbate O_3 pollution (heatwave penalty) due to unfavorable meteorology, short-term emission control according to the weather forecast would be expeditious to mitigate O_3 extremes. In the long term, with the surface transitioning toward NO_x-sensitive, this penalty is expected to even reverse into O_3 reduction as heatwave-enhanced dispersion outweighs its adverse effect on O_3 formation. When NO_x emissions decrease by 80%, heatwaves lower surface O_3 by 12.9% compared with normal days. In the upper urban boundary layer, the heatwave penalty also diminishes as reduced upward mixing of O_3 and NO_x limits O_3 production and accumulation (Extended Data Fig. 6c). Consequently, O_3 pollution gets progressively alleviated, indicating that urban emissions control can reduce the likelihood that heatwaves develop into compound climate and air pollution extremes.

Mitigating compound heat–ozone extremes in a warming climate

In the past decade, China has steadily reduced anthropogenic NO_x emissions by enforcing two phases (2013–2017 and 2018–2020) of clean air actions[31]. Although it has partly altered the surface O_3 photochemical regime, the VOC-sensitive regime and photochemical stratification remain widespread in megacities[32,33] (Extended Data Fig. 7a). The health and environmental burdens triggered by heatwave–O_3 associations thus threaten the climate resilience of city clusters, particularly amid accelerated climate change, urbanization and population aging.

Under the medium greenhouse gas emission scenario (Shared Socioeconomic Pathway (SSP) 2-4.5), which approximates current climate commitments, the surface daily maximum temperatures in China are projected to increase by over 1.5 °C and urban areas to expand by 1.4×10^4 km^2 (12.1%) in the coming decades (Fig. 4a), causing an escalation of urban heatwave extremes and the associated O_3 pollution. If applying lax emission policies without additional climate or air quality target constraints (2060 Baseline), China's major city clusters (that is, NCP, YRD, SCB and PRD) remain hotspots subject to concurrent heatwave and O_3 pollution, with the co-occurrence frequency during warm season rising to 9.5 days per year, 15.3 days per year, 8.4 days per year and 3.5 days per year by 2060, respectively, highlighting an urgent need for mitigating such compound risks (Fig. 4c). To combat climate change, China has committed to peak carbon dioxide emissions before 2030 and achieve carbon neutrality before 2060[34]. As cities account for more than 70% of carbon emissions and energy consumption, a transition to low-carbon energy and sustainable cities is a key solution[35], which will gain synergistic reductions in urban pollutant emissions given the shared emission sources[36] (Extended Data Fig. 8).

https://doi.org/10.1038/s44284-025-00302-1

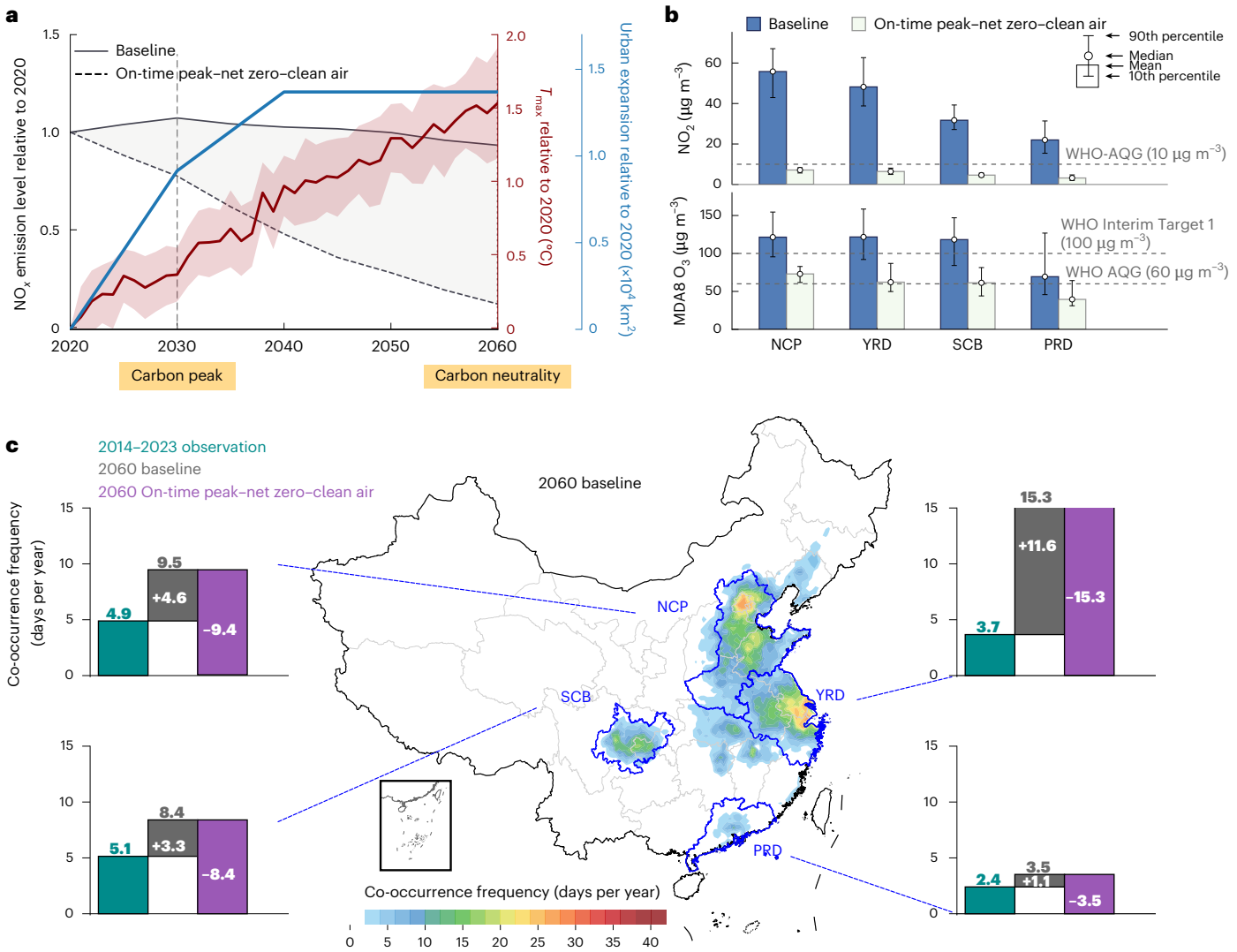

Fig. 4 | Future co-occurrence of heatwave and O_3 extremes during the warm season. a, Trends in China's NO_x emissions under the baseline scenario and on-time peak-net zero-clean air scenario, along with the daily maximum temperature (red line) and urban areas (blue line) under the SSP 2-4.5 scenario from 2020 to 2060. The daily maximum temperature is presented as mean ± 50% s.d. of 30 global climate models. **b**, Warm-season NO_2 concentrations and MDA8 O_3 levels under heatwaves across four city clusters (NCP, YRD, SCB and PRD) under the 2060 baseline and on-time peak-net zero-clean air scenarios. The bars show the mean concentrations across city clusters from a 4 month (123 days) simulation. The circles show the median values and the error bars present the 10th and 90th percentiles. The dashed gray lines represent the WHO Interim Target 1 and AQG. **c**, The spatial distribution of heatwaves and O_3 pollution co-occurrence frequency (days per year) during May–August under the 2060 baseline scenario in China and the comparison of co-occurrence frequencies between the recent decade and 2060. The gray and purple bars indicate the impacts of climate change and emission control, respectively.

Compared with the Baseline scenario, China's NO_x emissions are estimated to reduce by around 87.1% by 2060 owing to carbon neutrality and air pollution control policies (2060 on-time peak-net zero-clean air) (Fig. 4a).

On the basis of meteorology–chemistry modeling, it is estimated that the steep emission reductions owing to carbon neutrality policies could lower the warm-season NO_2 concentrations by 82.6–85.9% compared with the baseline scenario in 2060, falling below the World Health Organization (WHO) air quality guideline (AQG) level of 10 μg m^{-3} (Fig. 4b). As mentioned previously, this anthropogenic emissions reduction will shift O_3 photochemical regimes in megacities toward NO_x sensitivity and narrow its vertical disparities, enabling the further alleviation of heatwave-associated O_3 pollution by reducing photochemical production (Extended Data Fig. 7b–d). Quantitatively, the MDA8 O_3 levels under heatwaves could decrease by 50.3 μg m^{-3} (40.9%), 59.2 μg m^{-3} (47.4%), 53.4 μg m^{-3} (43.3%) and 33.2 μg m^{-3} (43.2%) in the four city clusters (NCP, YRD, SCB and PRD), respectively, where the NCP, YRD and SCB regions will meet the WHO Interim Target 1 of 100 μg m^{-3} and PRD will achieve stricter AQG targets of 60 μg m^{-3}. Although anthropogenic VOC (AVOC) emissions may also decrease via future end-of-pipe technologies and energy transitions, further analysis shows that NO_x reductions play a dominant role in O_3 pollution mitigation, accounting for 74.2–89.9% of the total reduction (Extended Data Fig. 8e,f). Consequently, the frequency of heatwaves and O_3 pollution co-occurrence during the warm season is expected to drop sharply to less than 0.1 days per year by 2060, despite plausible increase in heatwave frequency by more than 19.0 days per year. These results highlight the importance of urban emission control in mitigating compound heat–air pollution extremes.

Discussion

Our findings reveal that heatwaves tend to alter the vertical heterogeneity of precursors (that is, NO_x) as well as the photochemical regime, thus exacerbating O_3 pollution through more effective chemical

production both at the surface and aloft. Despite intensifying heatwaves, anthropogenic emissions can influence whether a meteorological extreme evolves into a compound air pollution hazard, especially in populated cities. In the short term, strategic emission reductions based on near real-time weather and air quality forecasts (for example, targeting more reduction under heatwave extremes) could alleviate O_3 pollution in a cost-effective way. In the long run, emission reductions entailed in China's carbon neutrality pledge could substantially mitigate heatwaves and O_3 pollution co-occurrence, even under a warming climate.

Our results are primarily based on in situ measurements and meteorology–chemistry model simulations, yet several heat-related aspects warrant further investigation. First, the single-day heatwave definition adopted here serves as a practical compromise between study motivation and the limitations of vertical observations. It reasonably captures daytime heat anomalies that drive turbulence and photochemistry, aligning with our focus on the subdiurnal meteorology–chemistry coupling processes. Second, AVOCs are also sensitive to temperature[37] and may contribute to O_3 formation[38]. On the basis of the observation analysis, we found that AVOCs accumulate more at night but do not exhibit a noticeable daytime increase (Extended Data Fig. 4d). However, vertical in situ measurements of VOCs are challenging and their role in heatwave and O_3 extremes still needs further exploration. In addition, beyond the inherent complexity of chemical and physical processes in compound heat–O_3 extremes, their intricate feedback with climate policies and socioeconomic activities adds further complexity[24]. For instance, dynamic emissions owing to heat-induced anthropogenic activity changes (that is, restricted outdoor labor and increasing energy demand) are not represented in the static inventories, possibly introducing uncertainties in this assessment.

Overall, the intricate interplay between meteorological, chemical and social processes underscores the imperative of understanding the extent to which humans can determine the escalation of weather extremes into compound extremes. While our findings are rooted in China's megacities, similar challenges confront other rapidly urbanizing regions such as the global south, where reliance on fossil fuels and inadequate energy transition technologies may exacerbate future NO_x emissions and compound risks[39]. This study therefore provides a valuable preview and model for emerging cities to recognize and address the foreseeable challenges of climate change and air pollution, enhancing their climate resilience and sustainability in a warming future.

Methods

Observational and reanalysis data

Ground-based observations of NO_2 and O_3 at more than 1,500 stations for the past 10 years (2014–2023) are archived at the air monitoring data center of the Ministry of Ecology and Environment of China, which were collected to analyze the spatial distribution characteristics. Tropospheric NO_2 and formaldehyde (HCHO) column density with a pixel size of approximately 13 × 24 km^2 were retrieved from the ozone monitoring instrument mounted on the Aura satellite[40].

We used hourly 2 m air temperature with a spatial resolution of 0.25° × 0.25° from the fifth-generation European Centre for Medium-Range Weather Forecasts reanalysis dataset (ERA5) to calculate the daily maximum temperature (T_{max})[41]. The data for 1969–2019 were used to calculate the present heatwave threshold, and data for 2014–2023 were paired with station observations of O_3 to determine heatwave–O_3 co-occurrences. Surface downward shortwave radiation flux, surface latent heat flux, 2 m air temperature and PBLH from the ERA5 were also used in the analysis.

Maximum near-surface air temperatures for 2020–2060 under scenario SSP 2-4.5 were obtained from the NASA Earth Exchange Global Daily Downscaled Projections (NEX-GDDP CMIP6) dataset[42] and used to identify future heatwaves. This dataset provides bias-corrected statistically downscaled data at 0.25° horizontal resolution from Coupled Model Intercomparison Project Phase 6 (CMIP6) as procurable from 35 global climate models. Considering the availability of the variable (maximum near-surface air temperatures) and scenario (SSP 2-4.5), 30 global climate models (Supplementary Table 1) were selected.

There is no universal definition for heatwaves yet. In this study, we defined a heatwave day using the 90th percentile of T_{max}, which is calculated using a 15 day moving window centered on each calendar day, based on 1969–2019 ERA5 data for the present and 2020–2060 CMIP6 projections for the future. This relative standard accounts for high spatiotemporal temperature variability and better reflects extreme heatwaves under future climatic conditions. It should be noted that the threshold criterion is a single day, rather than consecutive days, as we want a reasonable sample size with limited field observations to ensure a more robust analysis, as shown in Supplementary Fig. 1. Therefore, heatwave–O_3 co-occurrence is a day in which T_{max} exceeds its 90th threshold and MDA8 O_3 concentration exceeds 160 μg m^{-3}.

Airship field campaign

The airship field campaign was part of a multiplatform observation study of complex air pollution in the megacity cluster of eastern China, aiming to investigate the underlying causes of urban O_3 pollution during the warm season. The experiment was conducted at the Xianlin Campus of Nanjing University (32° 06′ N, 118° 57′ E) from 7 May 2023 to 28 June 2023. The airship platform consists of a tethered mega-balloon and customized rack for instrument deployment. It can record a vertical profile from surface to ceiling altitude of 1,200 m within 20–30 min as well as hover at a specified altitude, which allows for flexible vertical measurements and high temporal resolution. Owing to limitations such as precipitation, fierce wind and aviation control, we were unable to perform the vertical measurements at all times and ended up measuring 197 vertical profiles.

The airship deployed multiple instruments to record O_3, VOCs, reactive nitrogen species and other key pollutants. Meteorological parameters and gas species (O_3, NO and NO_2) were measured with a temporal resolution of 1 min. Ambient NO and NO_2 were measured by an NO_x analyzer (Thermo Scientific, Model 42i Trace Level) via the gas-phase chemiluminescence method. O_3 was measured by a 2B Technologies Personal Ozone Monitor and O_3 analyzer (Thermo Scientific, Model 49i) at different periods. Meteorological parameters, including relative humidity, wind speed, wind direction, pressure and air temperature were recorded by an Integrated CO_2 and H_2O Open-Path Gas Analyzer and 3-D Sonic Anemometer (IRGASON). In addition, high-frequency measurements (time resolution of 5 min) of VOCs and their oxidation products were conducted from 12 June to 16 June using the Vocus proton-transfer reaction time-of-flight mass spectrometer (Vocus PTR-ToF-MS, 2R), which improves the detection efficiency of product ions compared with conventional PTR instruments and is sensitive to a large range of oxygenated VOCs.

Surface measurements of aerosols, trace gases, VOCs and meteorological parameters were conducted synchronously at the SORPES station, which is located near the airship platform and is a representative urban site in the YRD region. Trace gases (SO_2, O_3, NO_x and CO) were continuously measured using a Thermo TEI 43i, TEI 49i, TEI 42i or TEI 48i, respectively. Meteorological parameters were measured at a height of 4 m from the meteorological tower and a ceilometer (CL51, Vaisala) was used to provide backscattered signals and PBLH. Non-methane hydrocarbons with 56 species and C2–C6 oxygenated VOCs were measured by a gas chromatograph–mass spectrometer/flame ionization detector (GC–MS/FID) system coupled with a cryogen-free preconcentration device. The time resolution was 1 h, and ambient air was sampled during the first 5 min of each hour for both channels. The uncertainties for VOCs measurements by the GC–MS/FID system are estimated to be 15–20%.

Observation-based model

A zero-dimensional observation-based box model (the framework for 0-D atmospheric modeling; F0AM) was used to simulate O_3 sensitivity[43]. This model adopts the gas-phase chemical mechanism Master Chemical Mechanism (MCM v3.3.1) that explicitly describes the degradation pathways of 143 primary VOCs, more than 5,900 species and 17,000 reactions, and also incorporates physical processes, including solar evolution, planetary boundary layer evolution, dry deposition and dilution[44]. In this study, averaged surface measurements of meteorological parameters (air temperature, relative humidity, pressure and boundary layer height) and chemical species (O_3, CO, SO_2, NO, NO_2, HONO and VOCs) obtained at the SORPES station during May–June 2023 were used to constrain the simulation and serve as the base scenario. The major VOCs observed by GC–MS/FID are presented in Supplementary Table 2. CH_4 and H_2 mixing ratios were assumed to be 1.9 ppm and 550 ppb, respectively. The photolysis frequencies (*J* values) were calculated by the National Center for Atmospheric Research tropospheric ultraviolet and visible radiation transfer model, which considers the influence of solar zenith angle, elevation, ground albedo and vertical O_3 column. We further scaled the *J* values according to the observed cloud cover and the observed NO/NO_2 ratio. Before running the base scenario, we conducted a 3 day model spin-up to initialize the unmeasured compounds. Then we proportionately increased or decreased the VOCs and NO_x concentrations from the base scenario to cover the practical VOCs and NO_x levels. Meanwhile, other conditions, including photolysis frequencies, temperature and relative humidity, were kept the same as the base scenario. The model results were interpolated into an isopleth for illustrating the impact of changes in NO_x and VOCs on the daily maximum O_3 concentrations, also known as the empirical kinetic modeling approach isopleth diagram. The performance of the base scenario is shown in Supplementary Fig. 2.

The O_3 photochemical regimes on normal days at the surface and around 1,000 m altitude were determined using averaged NO_x and the VOC observations from the SORPES station and airship platform. Owing to the limited availability of vertical VOC measurements, the direct calculation of the OH reactivity of VOCs, which is defined as the concentrations of VOCs multiplied by their respective reaction rate coefficients with OH, was not robust. Therefore, we utilized all VOC observations (excluding data with wind speeds greater than 5 m s^{-1}) to characterize the vertical distribution of VOCs and derived the surface OH reactivity of VOCs ($R_{VOCs_}$surface) from SORPES observations. The OH reactivity of VOCs near 1 km ($R_{VOCs_}$1 km) was then extrapolated as follows:

$$\frac{R_{VOCs\_}1\text{km}}{R_{VOCs\_}\text{surface}} = \frac{C_{VOCs\_}1\text{km\_Vocus}}{C_{VOCs\_}\text{surface\_Vocus}}$$

Here $C_{VOCs_}$surface_Vocus and $C_{VOCs_}$1km_Vocus represent the sum of BVOC (isoprene) and oxygenated VOC (that is, MVK, MACR and methylglyoxal) concentrations at the surface and around the altitude of 1,000 m measured by Vocus, respectively. Alkanes were not included here because they are a comparably minor and relatively unreactive fraction of total VOC, and the PTR method used by Vocus is not sensitive to alkanes.

The VOC reactivity and NO_x concentrations on heatwave days were obtained by adding heatwave-induced changes to the results for normal days. Heatwave-induced changes in VOCs and NO_x were estimated from the difference between the sensitivity experiments of the single-column model (see 'Meteorology–chemistry coupled simulations' section). This approach eliminates the uncertainties caused by daily variations in airship sampling heights and times between heatwave days and normal days. Although this derivation carries some uncertainties, it provides a feasible way to qualitatively assess O_3 sensitivity in the absence of sufficient observational data.

Meteorology–chemistry coupled simulations

The WRF–Chem model (version 3.9.1) was applied to identify the major pathways of heatwave-induced O_3 exacerbation and assess the change of O_3 and heatwave co-occurrence under future scenarios. This model considers a variety of physical and chemical processes, such as the emission and deposition of pollutants, advection and diffusion, gaseous and aqueous chemical transformation, aerosol chemistry and dynamics[45]. In addition, it embeds a diagnostic analysis tool to calculate the variations of O_3 concentrations induced by individual physical and chemical processes at each integration step, which have been successfully adopted in our previous work[46].

The major pathways of heatwave-induced O_3 changes were quantified using the SCM, which is a one-dimensional, idealized model including all physical and chemical processes in the regional version of WRF–Chem except for horizontal transport. Without the interference of the atmospheric three-dimensional dynamics, it is a key tool for understanding vertical physical and dynamic processes (land–atmospheric interaction, turbulence in PBL and so on) that drive heatwave events[47]. It provides a computationally efficient way to perform numerous numerical experiments and can be initialized by long-term observations at specific locations. Here, we designed six parallel numerical experiments to quantify the contribution of different processes on heatwave-induced O_3 exacerbation, with the first three affiliated with the HW (heatwave) group and the last three affiliated with the NM (normal) group (Supplementary Table 3).

For the HW group of simulations, averaged radiosonde measurements at 08:00 LT during the heatwave days in Nanjing were used as the initial meteorological fields to drive the model. HW_CTRL is the control simulation of this group, in which the impact of vertical turbulent mixing and biogenic emissions was excluded. On this basis, HW_Vmix incorporated the vertical mixing process and HW_Vmix_BVOC went a step further by considering biogenic emissions. The experiment designs of the NM group correspond individually to the HW group, but use averaged soundings from normal days to initialize the model. All experiments included anthropogenic emissions from the Multi-resolution Inventory for China, which were assumed constant without considering the heatwave-induced emission enhancement (for example, power plant emissions). More details about model configurations are provided in Supplementary Table 4.

By comparing the HW and NM group simulations with the aid of the diagnostic analysis tool, we calculated the O_3 change driven by vertical mixing ($Met\_O_3Vmix = Vmix_{\_HW\_Vmix\_BVOC} - Vmix_{\_NM\_Vmix\_BVOC}$) and chemical production processes ($Met\_O_3Chem = Chem_{\_HW\_Vmix\_BVOC} - Chem_{\_NM\_Vmix\_BVOC}$) in response to heatwave-induced meteorological anomalies. Enhanced chemical formation was subdivided into three crucial pathways: accelerated photochemical reaction rate due to high temperature and strong radiation ($PhotChem\_Rate = Chem_{\_HW\_CTRL} - Chem_{\_NM\_CTRL}$), vertical redistribution of anthropogenic precursors by reinforced turbulence ($Met\_NO_xVmix = Chem_{\_HW\_Vmix} - Chem_{\_NM\_Vmix} - PhotChem\_Rate$) and boosted BVOC emissions ($Emis\_BVOC = Chem_{\_HW\_Vmix\_BVOC} - Chem_{\_NM\_Vmix\_BVOC} - Met\_NO_xVmix$).

We utilized WRF–Chem modeling to perform a set of simulations to evaluate the heatwave and O_3 extremes and their co-occurrences in 2060 under different emission scenarios. The model domain covered all of China and its surrounding areas with a grid resolution of 27 km and 30 vertical layers. The simulations spanned the warm season (May–August) of 2060, with each run covering 5 days, and the chemical outputs from the preceding run were used as the initial conditions for the following one. The initial and boundary meteorological conditions were derived from the bias-corrected large-scale forcing climate model simulations of 2060 under scenarios from CMIP6 SSP 2-4.5, with a horizontal grid spacing of (1.25° × 1.25°) at 6 h intervals[48]. Key physical parameterizations included the Noah land surface scheme, the RRTMG radiation scheme and the Yonsei University PBL scheme,

whose combination allow more reliable and plausible descriptions of land–atmosphere interactions and vertical turbulent mixing processes in the PBL, enabling better simulation of surface temperatures and pollutants dispersion. For the chemical mechanisms, the carbon-bond photochemical mechanism combined with the Model for Simulating Aerosol Interactions and Chemistry aerosol module were utilized.

Natural emissions in both the single-column model and regional model were calculated by the Model of Emissions of Gases and Aerosols from Nature (MEGAN)[49], which estimates biogenic emissions online based on static parameters (for example, fraction of plant function type and leaf area index) provided by MODIS observations and real-time meteorological conditions (for example, temperature, solar radiation and soil moisture). This tight coupling between emission calculations and meteorological drivers makes the MEGAN well capable of capturing the temperature dependence of BVOC emissions[7]. It also calculates NO_x emissions from the soil nitrogen pool using a temperature-dependent rate. Given that soil NO_x emission rates depend not only on temperature but also other variables influencing nitrification/denitrification that vary with temperature (especially soil moisture), such simplification may underestimate the soil NO_x emissions.

Future anthropogenic emissions in 2060 were derived from an integrated assessment model GCAM (China-focused Global Change Assessment Model) and a technology-based emission projection model DPEC (the dynamic projection model for emissions in China)[36]. This model provides five scenario-specific air pollutants and CO_2 emissions for China, which considers the growing energy demand and low-carbon policy in power and industry sectors. We selected the baseline scenario and the on-time peak-net zero-clean air emissions scenario for further analysis. The two scenarios share the same socio-economic development roadmap, but the 2060 baseline scenario does not consider additional climate or air quality target constraints. By contrast, the on-time peak-net zero-clean air scenario deploys a range of carbon reduction measures during 2020–2030, a more ambitious low-carbon transition after 2030 and the optimal end-of-pipe pollution control during 2020–2060 to achieve carbon neutrality and air quality improvement. Such strict measures could reduce anthropogenic NO_x and non-methane volatile organic compound emissions by 64% and 87%, respectively. Therefore, the difference between the on-time peak-net zero-clean air and baseline represents the impact of anthropogenic endeavors on heatwave–O_3 co-occurrence extremes. On this basis, the only NO_x cut scenario reduces NO_x emissions to the on-time peak-net zero-clean air level while maintaining other emissions consistent with the baseline to isolate the contribution of anthropogenic NO_x control.

We validated the performance of the WRF–Chem model in capturing heat and O_3 pollution extremes using available meteorology and air quality observations. As illustrated in Supplementary Figs. 3 and 4, the baseline simulation during the 2023 airship campaign shows good performance in capturing the magnitude and hourly variation of meteorological parameters and pollutants at the campaign site, as well as the temperature and O_3 anomalies during heatwaves across major urban clusters. In addition, we further evaluated the impact of different chemical mechanisms in the model on future O_3 predictions. We conducted an additional simulation using the common reactive intermediates gas-phase chemical mechanism. As shown in Supplementary Fig. 5, carbon-bond photochemical mechanism and common reactive intermediate simulations show reasonably consistent O_3 levels and temporal variations across major city clusters, with modest differences in MDA8 O_3 especially at high temperatures, indicating the robustness of future O_3 predictions under a changing climate and precursor levels.

Reporting summary

Further information on research design is available in the Nature Portfolio Reporting Summary linked to this article.

Data availability

The data that supporting the findings of this study are available via GitHub at https://github.com/Xueyu07/compound_heat-ozone_extremes.git. The shapefile data in all maps were generated using open-source Python software and the cnmaps package available via GitHub at https://github.com/cnmetlab/cnmaps. The ground-level O_3 observation data were obtained from the China National Environmental Monitoring Centre at http://www.cnemc.cn/en/. The hourly meteorological data were obtained from the National Meteorological Information Center of the China Meteorological Administration at http://data.cma.cn/en. The current and future air temperatures data are available at https://cds.climate.copernicus.eu/datasets/reanalysis-era5-land?tab=overview and https://nex-gddp-cmip6.s3.us-west-2.amazonaws.com/index.html#NEX-GDDP-CMIP6/.

Code availability

The F0AM source code can be downloaded via GitHub at https://github.com/AirChem/F0AM. The cnmaps package is publicly available via GitHub at https://github.com/cnmetlab/cnmaps. The source code of the WRF–Chem model is archived on the UCAR data repository at http://www2.mmm.ucar.edu/wrf/users/download. The Python codes for generating main results are available via GitHub at https://github.com/Xueyu07/compound_heat-ozone_extremes.git.

References

1. Watts, N. et al. The 2020 report of The Lancet Countdown on health and climate change: responding to converging crises. *Lancet* **397**, 129–170 (2021).
2. Li, S. et al. Mitigating climate change and ozone pollution will improve Chinese food security. *One Earth* **8**, 101166 (2024).
3. Schnell, J. L. & Prather, M. J. Co-occurrence of extremes in surface ozone, particulate matter, and temperature over eastern North America. *Proc. Natl Acad. Sci. USA* **114**, 2854–2859 (2017).
4. Wang, T. et al. Pro-thrombotic changes in response to ambient ozone exposure exacerbated by temperatures. *Environ. Sci. Technol.* **59**, 8391–8401 (2025).
5. Pusede, S. E., Steiner, A. L. & Cohen, R. C. Temperature and recent trends in the chemistry of continental surface ozone. *Chem. Rev.* **115**, 3898–3918 (2015).
6. Barnes, P. W. et al. Ozone depletion, ultraviolet radiation, climate change and prospects for a sustainable future. *Nat. Sustain.* **2**, 569–579 (2019).
7. Li, M. et al. Coping with the concurrent heatwaves and ozone extremes in China under a warming climate. *Sci. Bull.* **69**, 2938–2947 (2024).
8. Gao, M. et al. Large-scale climate patterns offer preseasonal hints on the co-occurrence of heat wave and O_3 pollution in China. *Proc. Natl Acad. Sci. USA* **120**, e2218274120 (2023).
9. Steiner, A. L. et al. Observed suppression of ozone formation at extremely high temperatures due to chemical and biophysical feedbacks. *Proc. Natl Acad. Sci. USA* **107**, 19685–19690 (2010).
10. Wang, H. et al. Heat waves may trigger unexpected surge in aerosol and ozone precursor emissions from sedges in urban landscapes. *Proc. Natl Acad. Sci. USA* **121**, e2412817121 (2024).
11. Lin, M. et al. Vegetation feedbacks during drought exacerbate ozone air pollution extremes in Europe. *Nat. Clim. Change* **10**, 444–451 (2020).
12. Qi, C. et al. Impacts of tropical cyclone–heat wave compound events on surface ozone in eastern China: comparison between the Yangtze River and Pearl River deltas. *Atmos. Chem. Phys.* **24**, 11775–11789 (2024).
13. Luo, Y. et al. A mechanism of stratospheric O_3 intrusion into the atmospheric environment: a case study of the North China Plain. *Atmos. Chem. Phys.* **24**, 7013–7026 (2024).

14. Wang, N. et al. Typhoon-boosted biogenic emission aggravates cross-regional ozone pollution in China. *Sci. Adv.* **8**, eabl6166 (2022).
15. Xu, Z. et al. Impact of biomass burning and vertical mixing of residual-layer aged plumes on ozone in the Yangtze River Delta, China: a tethered-balloon measurement and modeling study of a multiday ozone episode. *J.Geophys. Res. Atmos.* **123**, 11,786–11,803 (2018).
16. Benish, S. E. et al. Measurement report: aircraft observations of ozone, nitrogen oxides, and volatile organic compounds over Hebei Province, China. *Atmos. Chem. Phys.* **20**, 14523–14545 (2020).
17. Hotz, B., Papritz, L. & Röthlisberger, M. Understanding the vertical temperature structure of recent record-shattering heatwaves. *Weather Clim. Dynam.* **5**, 323–343 (2024).
18. Schumacher, D. L., Hauser, M. & Seneviratne, S. I. Drivers and mechanisms of the 2021 Pacific Northwest heatwave. *Earth's Futur.* **10**, e2022EF002967 (2022).
19. Gaudel, A. et al. Tropospheric ozone assessment report: present-day distribution and trends of tropospheric ozone relevant to climate and global atmospheric chemistry model evaluation. *Elementa* **6**, 39 (2018).
20. Bai, X., Shi, P. & Liu, Y. Society: realizing China's urban dream. *Nature* **509**, 158–160 (2014).
21. Wang, H. et al. Deciphering decadal urban ozone trends from historical records since 1980. *Natl Sci. Rev.* **11**, nwae369 (2024).
22. Sun, Y., Zhang, X., Ren, G., Zwiers, F. W. & Hu, T. Contribution of urbanization to warming in China. *Nat. Clim. Change* **6**, 706–709 (2016).
23. Xiao, X. et al. Amplified upward trend of the joint occurrences of heat and ozone extremes in China over 2013–20. *Bull. Am. Meteorol. Soc.* **103**, E1330–E1342 (2022).
24. Chen, T., Wang, T., Xue, L. & Brasseur, G. Heatwave exacerbates air pollution in China through intertwined climate–energy–environment interactions. *Sci. Bull.* **69**, 2765–2775 (2024).
25. Lu, X. et al. The underappreciated role of agricultural soil nitrogen oxide emissions in ozone pollution regulation in North China. *Nat. Commun.* **12**, 5021 (2021).
26. Liu, S. et al. Underappreciated emission spikes from power plants during heatwaves observed from space: case studies in India and China. *Earth's Futur.* **12**, e2023EF003937 (2024).
27. Wouters, H. et al. Soil drought can mitigate deadly heat stress thanks to a reduction of air humidity. *Sci. Adv.* **8**, eabe6653 (2022).
28. Zhou, S. et al. Land–atmosphere feedbacks exacerbate concurrent soil drought and atmospheric aridity. *Proc. Natl Acad. Sci. USA* **116**, 18848–18853 (2019).
29. Domeisen, D. I. V. et al. Prediction and projection of heatwaves. *Nat. Rev. Earth Environ.* **4**, 36–50 (2023).
30. Hong, Q. et al. Inferring vertical variability and diurnal evolution of O_3 formation sensitivity based on the vertical distribution of summertime HCHO and NO_2 in Guangzhou, China. *Sci. Total Environ.* **827**, 154045 (2022).
31. Zheng, B. et al. Trends in China's anthropogenic emissions since 2010 as the consequence of clean air actions. *Atmos. Chem. Phys.* **18**, 14095–14111 (2018).
32. Ren, J., Guo, F. & Xie, S. Diagnosing ozone–NO_x–VOC sensitivity and revealing causes of ozone increases in China based on 2013–2021 satellite retrievals. *Atmos. Chem. Phys.* **22**, 15035–15047 (2022).
33. Zhu, S. et al. Shifts of formation regimes and increases of atmospheric oxidation led to ozone increase in North China Plain and Yangtze River Delta from 2016 to 2019. *J. Geophys. Res. Atmos.* **128**, e2022JD038373 (2023).
34. Mallapaty, S. How China could be carbon neutral by mid-century. *Nature* **586**, 482–483 (2020).
35. Kammen, D. M. & Sunter, D. A. City-integrated renewable energy for urban sustainability. *Science* **352**, 922–928 (2016).
36. Cheng, J. et al. A synergistic approach to air pollution control and carbon neutrality in China can avoid millions of premature deaths annually by 2060. *One Earth* **6**, 978–989 (2023).
37. Wu, W. et al. Temperature-dependent evaporative anthropogenic VOC emissions significantly exacerbate regional ozone pollution. *Environ. Sci. Technol.* **58**, 5430–5441 (2024).
38. Qin, M. et al. Increased urban ozone in heatwaves due to temperature-induced emissions of anthropogenic volatile organic compounds. *Nat. Geosci.* **18**, 50–56 (2025).
39. Vohra, K. et al. Rapid rise in premature mortality due to anthropogenic air pollution in fast-growing tropical cities from 2005 to 2018. *Sci. Adv.* **8**, eabm4435 (2022).
40. Boersma, K. F. et al. Near-real time retrieval of tropospheric NO_2 from OMI. *Atmos. Chem. Phys.* **7**, 2103–2118 (2007).
41. Hersbach, H. et al. The ERA5 global reanalysis. *Q. J. R. Meteorol. Soc.* **146**, 1999–2049 (2020).
42. Thrasher, B. et al. NASA global daily downscaled projections, CMIP6. *Sci. Data* **9**, 262 (2022).
43. Wolfe, G. M., Marvin, M. R., Roberts, S. J., Travis, K. R. & Liao, J. The framework for 0-D atmospheric modeling (F0AM) v3.1. *Geosci. Model Dev.* **9**, 3309–3319 (2016).
44. Xue, L. K. et al. Ground-level ozone in four Chinese cities: precursors, regional transport and heterogeneous processes. *Atmos. Chem. Phys.* **14**, 13175–13188 (2014).
45. Grell, G. A. et al. Fully coupled "online" chemistry within the WRF model. *Atmos. Environ.* **39**, 6957–6975 (2005).
46. Zhou, X. et al. Fast secondary aerosol formation in residual layer and its impact on air pollution over Eastern China. *J. Geophys. Res. Atmos.* **128**, e2023JD038501 (2023).
47. Miralles, D. G., Teuling, A. J., van Heerwaarden, C. C. & Vilà-Guerau de Arellano, J.Mega-heatwave temperatures due to combined soil desiccation and atmospheric heat accumulation. *Nat. Geosci.* **7**, 345–349 (2014).
48. Xu, Z., Han, Y., Tam, C.-Y., Yang, Z.-L. & Fu, C. Bias-corrected CMIP6 global dataset for dynamical downscaling of the historical and future climate (1979–2100). *Sci. Data* **8**, 293 (2021).
49. Guenther, A. et al. Estimates of global terrestrial isoprene emissions using MEGAN (Model of Emissions of Gases and Aerosols from Nature). *Atmos. Chem. Phys.* **6**, 3181–3210 (2006).
50. Dijkstra, L. et al. Applying the degree of urbanisation to the globe: a new harmonised definition reveals a different picture of global urbanisation. *J. Urban Econ.* **125**, 103312 (2021).

Acknowledgements

This work was supported by the National Natural Science Foundation of China (grant no. 42293322 to A.D.), the National Key Research and Development Program of China (grant no. 2022YFC3701105 to X.H.) and the Fundamental Research Funds for the Central Universities (grant no. 14380234 to X.H.). We are grateful to the High-Performance Computing and Massive Data Center of Nanjing University for running the model on its Blade cluster system.

Author contributions

These authors contributed equally: X.Z. and M.L. X.H. and A.D. conceived the overall idea. X.Z., M.L. and X.H. performed most of the data analysis, model simulations and result interpretation. Z.W., T.L., J.W., X.C. and X.Q. collected and processed the observation campaign data. G.G. provided the emission inventory. X.H. and X.Z. wrote the paper with contributions from H.Z., Y.Q. and all the other co-authors.

Competing interests

The authors declare no competing interests.

Additional information

Extended data is available for this paper at https://doi.org/10.1038/s44284-025-00302-1.

Supplementary information The online version contains supplementary material available at https://doi.org/10.1038/s44284-025-00302-1.

Correspondence and requests for materials should be addressed to Xin Huang.

Peer review information *Nature Cities* thanks the anonymous reviewer(s) for their contribution to the peer review of this work.

https://doi.org/10.1038/s44284-025-00302-1

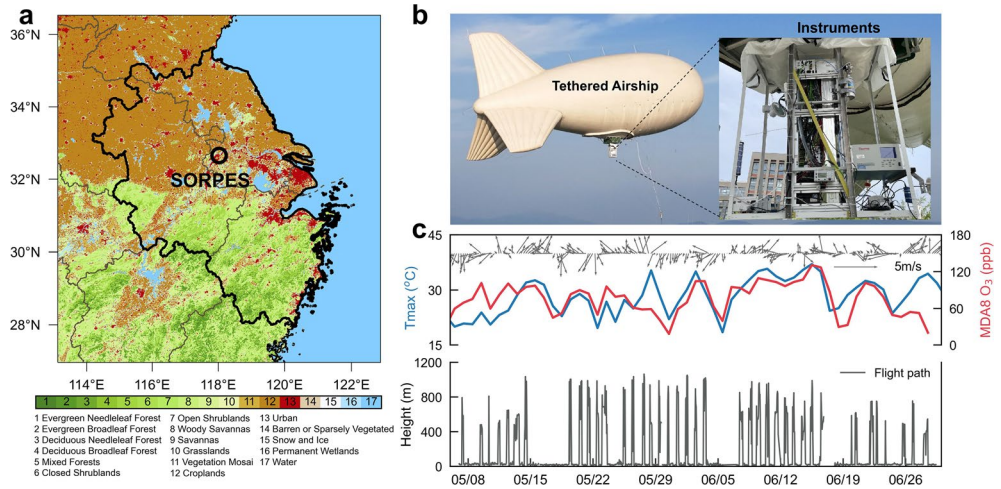

Extended Data Fig. 1 | Overview of the airship field campaign in Nanjing during May–June 2023. a, Location of the airship campaign site (SORPES) with the land cover types in the YRD region. **b**, Picture of the airship platform. **c**, Time series of daily maximum temperature (T_{max}) and MDA8 O_3 concentration as well as the flight path of the airship during the field campaign.

https://doi.org/10.1038/s44284-025-00302-1

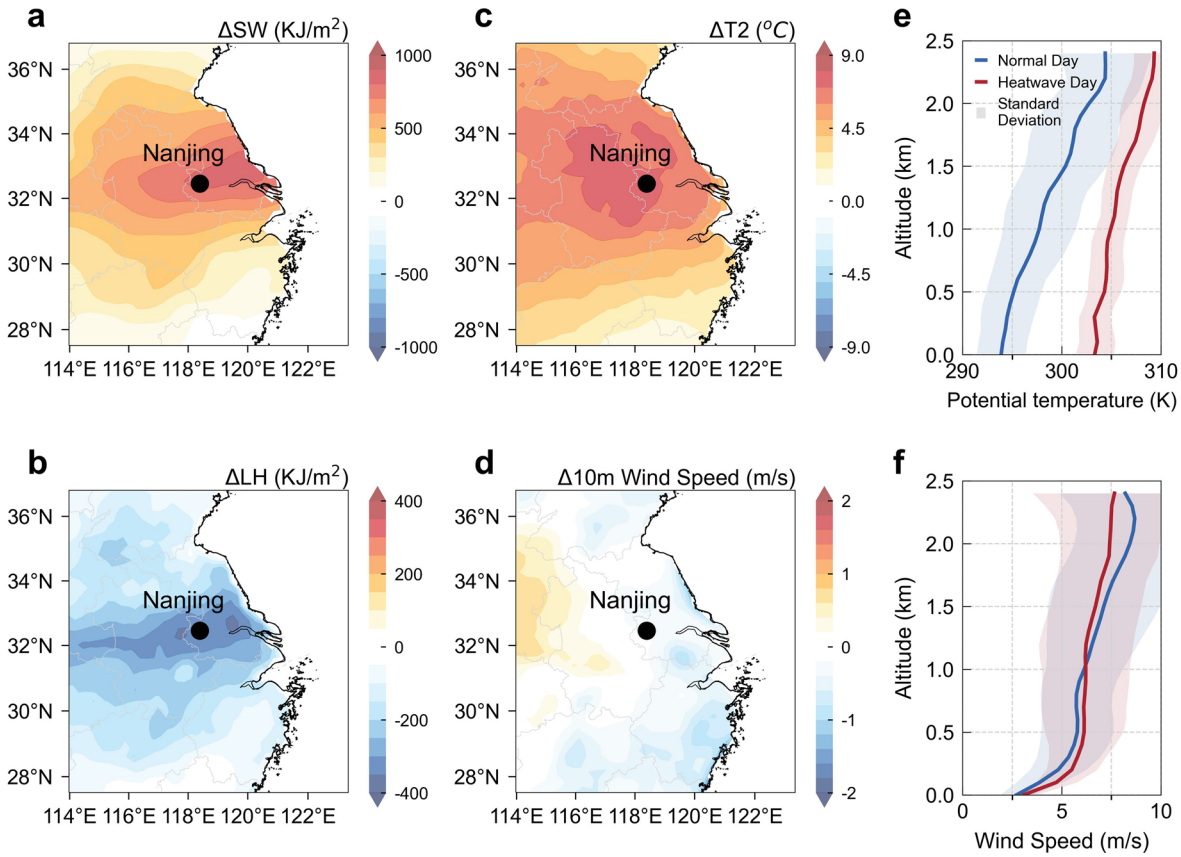

Extended Data Fig. 2 | Anomalies of meteorological variables during heatwaves in May–June 2023. a–d, Averaged difference of (**a**) surface downward shortwave radiation flux (SW), (**b**) surface latent heat flux (LH), (**c**) 2 m air temperature (T2), and (**d**) 10 m wind speed between heatwave days and normal days in Nanjing from ERA5 reanalysis data. **e**, **f**, Vertical profiles of (**e**) potential temperature and (**f**) horizontal wind speed at 20:00 LT in Nanjing obtained from Wyoming radiosonde measurements. Data are presented as mean ± 50% standard deviation. Potential temperature can indicate atmospheric turbulence when high-frequency wind measurements are unavailable, which distributes more evenly under stronger turbulence motion and shows greater vertical countergradient under stable conditions.

https://doi.org/10.1038/s44284-025-00302-1

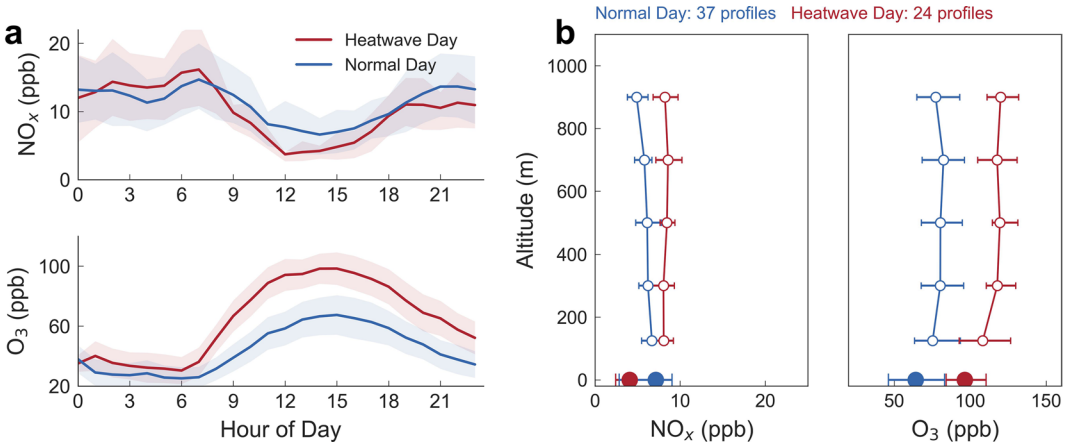

Extended Data Fig. 3 | Surface and vertical observation of O_3 and NO_x in Nanjing. a, Averaged diurnal variations of NO_x and O_3 for heatwave days and normal days during the warm season (May–August) in 2023. The shaded areas represent intervals of mean ± 50% standard deviation. **b**, Vertical profiles of average NO_x and O_3 concentrations in the afternoon (12:00–16:00 LT) during the field campaign. Circles indicate mean concentration and the error bars show the 25th and 75th percentiles, respectively. Normal day includes 37 profiles and heatwave day includes 24 profiles. Solid circles indicate mean surface concentrations with the error bars showing 25th and 75th percentiles for the afternoon during warm season in 2023.

https://doi.org/10.1038/s44284-025-00302-1

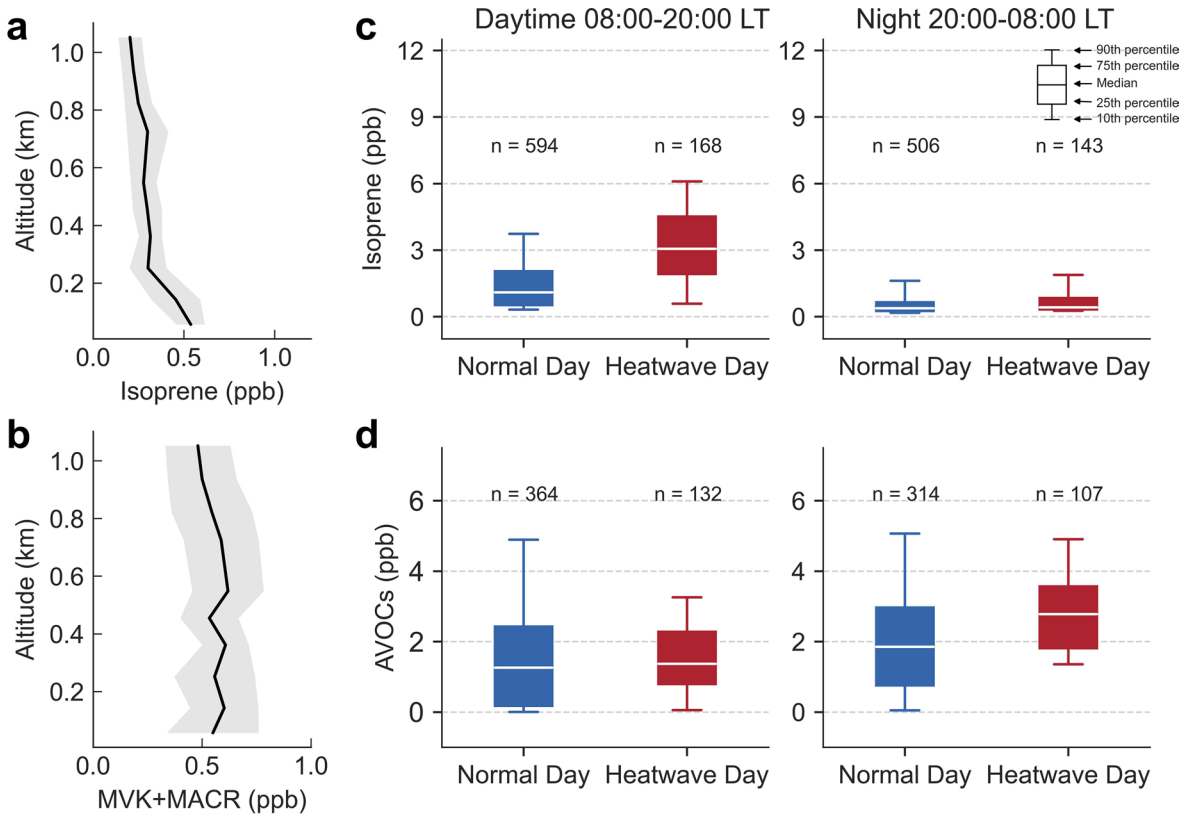

Extended Data Fig. 4 | Surface and vertical observation of major VOCs in Nanjing. a, **b**, Averaged profiles of (**a**) isoprene and (**b**) its oxidation products methyl vinyl ketone (MVK) and methacrolein (MACR) from 12 June to 16 June. The shaded areas represent intervals of mean ±50% standard deviation. Data with horizontal wind speeds greater than 5 m/s were removed to exclude the effect of potential transport. **c**, **d**, Comparison of daytime and nighttime concentration of (**c**) isoprene and (**d**) major AVOCs between normal days and heatwave days at SORPES during the airship experiment. The box plots indicate median (line), 25th and 75th percentiles (box), and 10th and 90th percentiles (whiskers). The number of observation points (n) is presented at the top of each figure. AVOCs calculated here include m/p-xylene, propene, t-2-butene, toluene, o-xylene, 1,3-butadiene, n-butane, propane, 1,2,4-trimethylbenzene, and n-decane.

https://doi.org/10.1038/s44284-025-00302-1

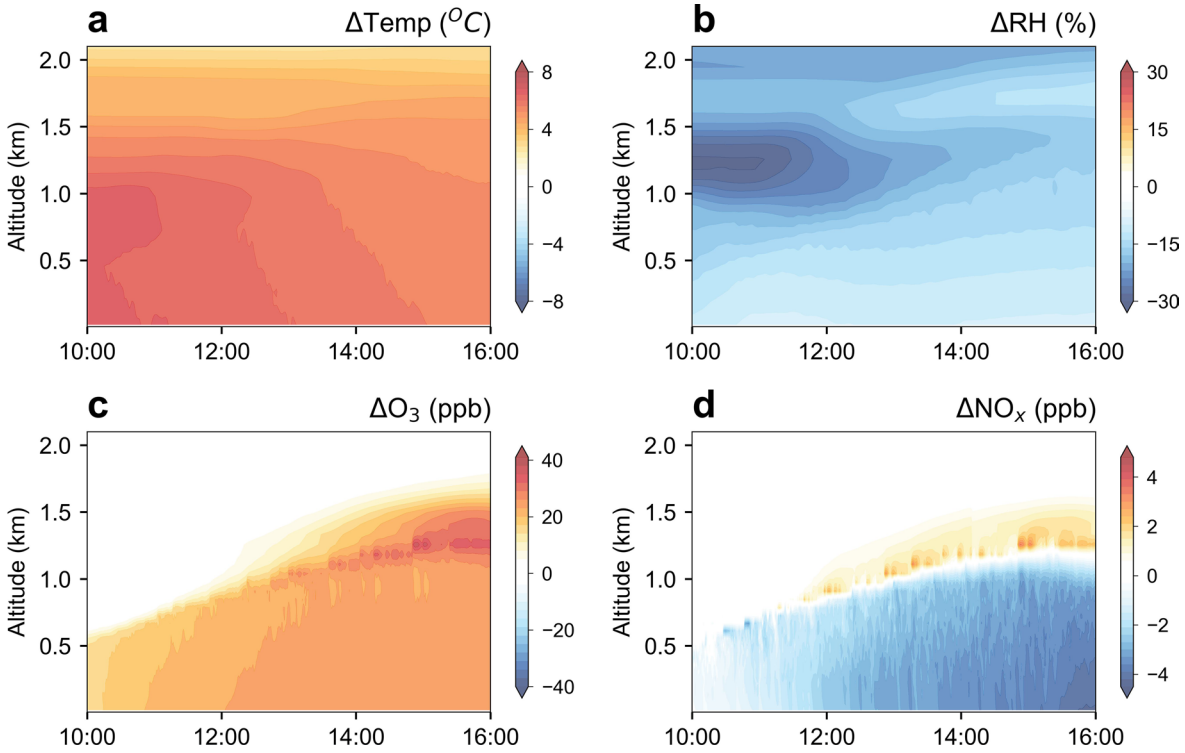

Extended Data Fig. 5 | Heatwave-induced meteorological and pollution differences simulated by 1-dimensional modeling. a–d, WRF-Chem SCM simulated vertical difference of (**a**) air temperature (Temp), (**b**) relative humidity (RH), (**c**) O_3, and (**d**) NO_x in Nanjing induced by heatwaves.

https://doi.org/10.1038/s44284-025-00302-1

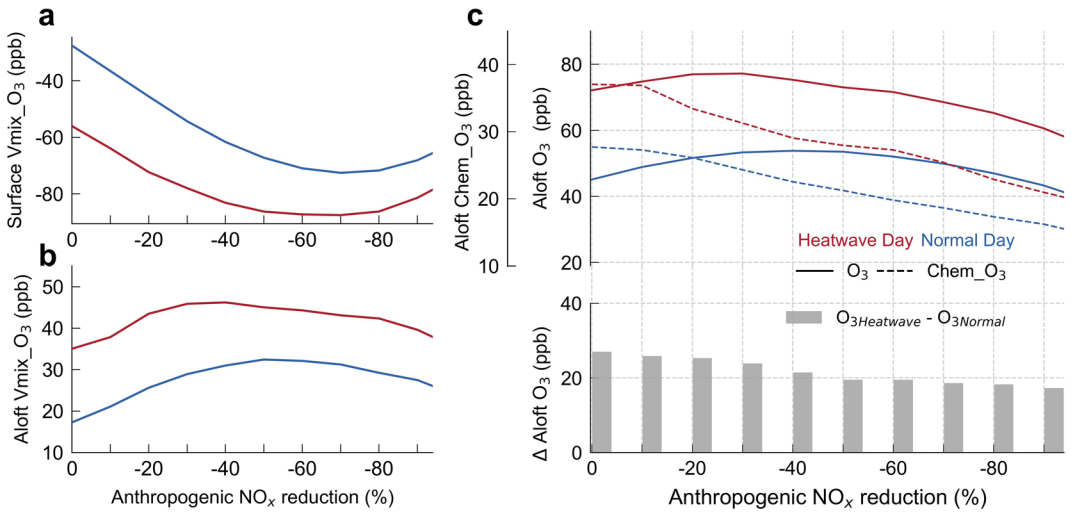

Extended Data Fig. 6 | Response of heatwave-induced daytime O_3 anomaly to NO_x emission reductions. a, **b**, Contribution of vertical mixing in daytime O_3 enhancement in response to anthropogenic NO_x emission reductions near the surface (<100 m, **a**) and aloft (1000–1500 m, **b**). **c**, Same as (Fig. 3b) but for aloft.

https://doi.org/10.1038/s44284-025-00302-1

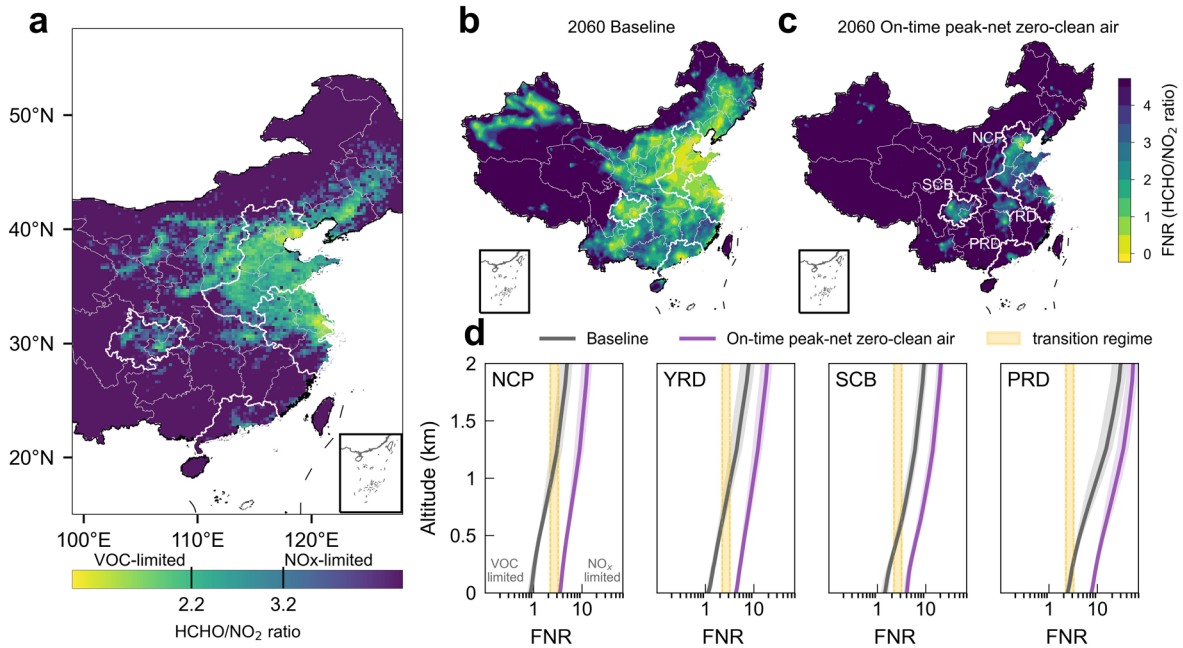

Extended Data Fig. 7 | Current O_3 photochemical regimes and future shifts. **a**, Spatial distribution of O_3 formation regimes derived from satellite-based $HCHO/NO_2$ ratio (FNR) during May–August over 2020–2023. **b**, **c**, Surface FNR distribution during the warm season under (**b**) 2060 Baseline scenario and (**c**) 2060 On-time peak-net zero-clean air scenario. **d**, Vertical profile of O_3 formation regimes in the four Chinese city clusters (NCP, YRD, SCB, PRD) by 2060 under different emission scenarios. FNR values are presented as mean ± 50% standard deviation. The O_3 photochemical regimes were identified using the FNR threshold (2.2–3.2).

https://doi.org/10.1038/s44284-025-00302-1

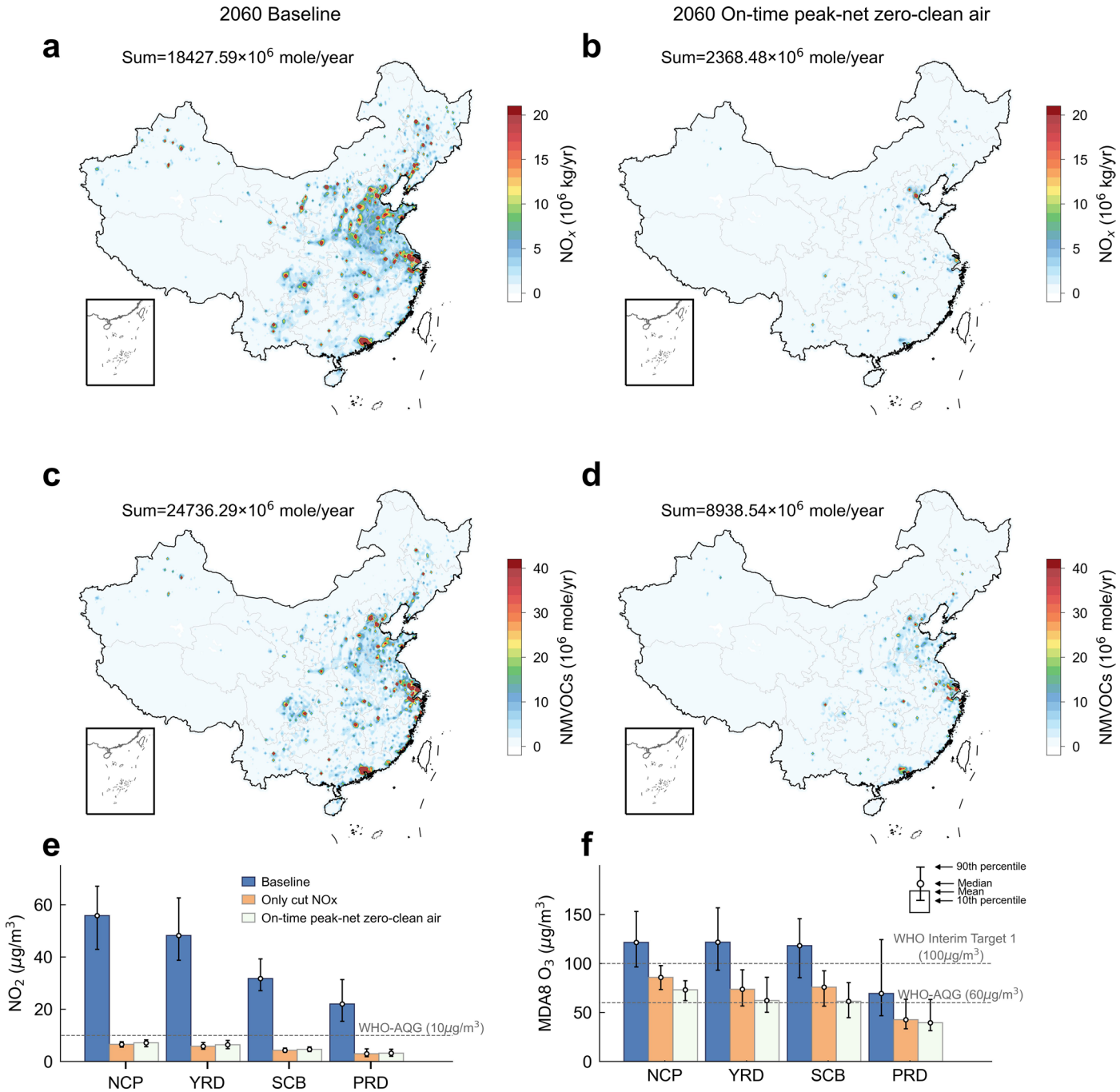

Extended Data Fig. 8 | Projections of anthropogenic emissions and pollutant concentrations under different emission scenarios in 2060. a, **b**, Distribution of NO_x emissions during the warm season under (**a**) 2060 Baseline scenario and (**b**) 2060 On-time peak-net zero-clean air scenario, respectively. **c**, **d**, Same as (**a**, **b**) but for NMVOCs. **e**, **f**, Warm-season NO_2 concentrations (**e**) and MDA8 O_3 concentrations (**f**) under heatwaves in four Chinese city clusters (that is, NCP, YRD, SCB, PRD) by 2060. The blue, orange, and white bars represent the Baseline, only cut NO_x (NO_x emissions follow the On-time peak-net zero-clean air and other emissions follow the Baseline) and On-time peak-net zero-clean air emission pathways, respectively. The bars show the mean concentrations across city clusters from four-month (123 days) simulation. The circles show the median values and the error bars present the 10th and 90th percentile.